Journal of Marine Systems 204 (2020) 103288

Contents lists available at ScienceDirect

Journal of Marine Systems

journal homepage: www.elsevier.com/locate/jmarsys

Weekly variability of hydrography and transport of northwestern inflows into the northern North Sea

Peter M.F. Sheehan[a,*], Barbara Berx[b], Alejandro Gallego[b], Rob A. Hall[a], Karen J. Heywood[a], Bastien Y. Queste[a,1]

[a] Centre for Ocean and Atmospheric Sciences, School of Environmental Sciences, University of East Anglia, Norwich Research Park, Norwich NR4 7TJ, United Kingdom
[b] Marine Scotland Science, 375 Victoria Road, Aberdeen AB11 9DB, United Kingdom

ARTICLE INFO

Keywords:
North Sea
Fair Isle Current
East Shetland Atlantic Inflow
Water masses
Transport
Ocean gliders

ABSTRACT

Quantifying the variability of North Sea inflows and understanding the temporal variability of their physical properties are essential for understanding, modelling and managing the ecosystems of the North Sea. The Joint North Sea Information System (JONSIS) line hydrographic section crosses the path of the main inflows of Atlantic water into the northwestern North Sea. We use observations from an autonomous underwater glider to observe the inflows at high spatial and temporal resolutions. The glider completed 10 partial sections of the JONSIS line in October and November of 2013. Key water masses of the inflow are identified; their spatial distribution varies greatly from section to section. This is not apparent from long-running ship surveys of the JONSIS line, which are generally several months apart. In particular, the distribution of water of most recent Atlantic origin varies as summer stratification decays throughout autumn: at the start of the deployment it is present as a thin layer beneath the thermocline; at the end of the deployment, it occupies the full depth of the water column. Thermohaline flow, i.e. that which is driven by horizontal density gradients, is focused into three or four jets (approximately 10 km wide). Jets as narrow as these have not previously been observed in the region. We also observe baroclinic eddies. The thermohaline transport of the inflows is compared with the absolute transport that is derived by referencing geostrophic shear to the glider's dive-average current. Thermohaline transport (approximately 0.2 Sv) is consistently smaller than absolute transport (approximately 0.5 Sv). The week-to-week variability in hydrography and flow structure identified in this study is relevant to on-going efforts to define a background state against which the nature of anthropogenic changes can be assessed, and future modelling efforts should represent the spatial and temporal variability that we have identified.

1. Introduction

The North Sea lies on the northwest European continental shelf and separates the United Kingdom from mainland Europe (Fig. 1). The North Sea is heavily managed and economically important, and maintaining the health of the region's ecosystem is recognised at national and supranational levels by the countries of the North Sea perimeter (e.g. EU, 2008). Consequently, in recent decades, regulation has become a key driver of efforts to better understand the physics, chemistry and biology of the North Sea (e.g. Emeis et al., 2015; Johnson, 2008). Inflow to the North Sea from the Atlantic Ocean occurs through the Fair Isle Current (FIC; 0.5 Sv; 1 Sv = 10^6 m^3 s^{-1}), the East Shetland Atlantic Inflow (ESAI; 0.5 Sv), the Norwegian Trench Inflow (1.2 Sv) and the English Channel Inflow (0.2 Sv; Fig. 1; volume transports from Winther and Johannessen, 2006). The waters of the Norwegian Trench Inflow retroflect largely within the Norwegian Trench (Furnes et al., 1986) and volume transport of the English Channel Inflow is considerably less than that of the other three inflows (Otto et al., 1990; Winther and Johannessen, 2006). Consequently, it is the FIC and ESAI, the northwestern inflows, that have the greatest effect on conditions in the northern North Sea. The hydrographic properties of inflowing water masses, combined with the rate of the inflow, exert a strong influence on a region's ecosystem (Beaugrand, 2004; Edwards et al., 2002; Holliday and Reid, 2001; Lindley et al., 1990) and are the means by which oceanic perturbations may propagate into the region (Dickson et al., 1988; Edwards et al., 2002; Holliday and Reid, 2001). An accurate physical description of the inflows is a prerequisite for developing reliable models of a region's water quality, biogeochemistry and

* Corresponding author.
E-mail address: p.sheehan@uea.ac.uk (P.M.F. Sheehan).
[1] Present address: Department of Marine Sciences, University of Gothenburg, Box 461, Gothenburg 40530, Sweden.

https://doi.org/10.1016/j.jmarsys.2019.103288
Received 12 August 2019; Received in revised form 16 December 2019; Accepted 17 December 2019
Available online 26 December 2019

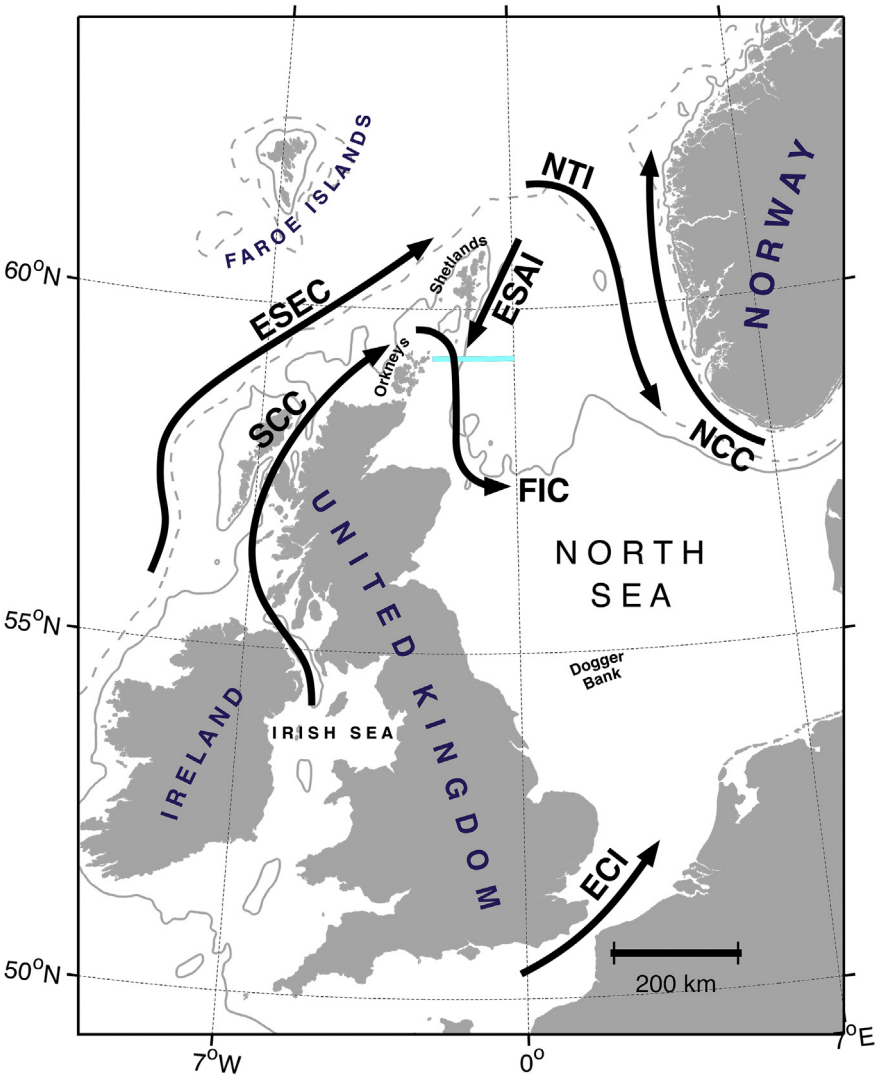

Fig. 1. Map of the North Sea. The location of the JONSIS line (light blue) and the approximate paths (black lines) of the Fair Isle Current (FIC), East Shetland Atlantic Inflow (ESAI), European Shelf Edge Current (ESEC), Scottish Coastal Current (SCC), Norwegian Coastal Current (NCC), Norwegian Trench Inflow (NTI) and English Channel Inflow (ECI) are shown (Marsh et al., 2017; Otto et al., 1990; Turrell, 1992). The 100 m isobath is indicated by the solid grey line and the 200 m isobath is indicated by the dashed grey line; land is shaded.

ecology (Skogen and Moll, 2005; Taylor, 1987; Turrell and Henderson, 1990), and for understanding potential contaminant pathways (du Bois, 1996; Taylor, 1987).

The FIC originates to the west of the Fair Isle Gap, the narrow sea passage between the Orkney and Shetland archipelagoes through which the current enters the North Sea (Fig. 1). It comprises a mixture of Atlantic water from the northward-flowing European Shelf Edge Current and low-salinity coastal water from around the complex island chains off the western coast of Scotland that is carried north by the Scottish Coastal Current (Fig. 1; Dooley, 1974; Hill et al., 1997; Inall et al., 2009; Marsh et al., 2017; Turrell et al., 1992). Within the North Sea, the path of the FIC has been traced southward from the Fair Isle Gap to approximately 57.5°N (Dooley, 1974; Turrell et al., 1992). The ESAI comprises water of more recent Atlantic origin (Turrell et al., 1992) and is fed by waters of the European Shelf Edge Current that cross onto the continental shelf to the north of the Shetlands (Turrell et al., 1996). Within the North Sea, the ESAI follows a similar path to the FIC (Turrell et al., 1992). The ESAI is a more diffuse flow than the FIC, but average transports in the two currents are of a similar magnitude (Winther and Johannessen, 2006).

Present understanding of the northwestern inflows is derived from ship surveys in the northern North Sea since at least the 1960s (González-Pola et al., 2019). One of the primary purposes of these surveys is long-term monitoring of the region, in order that trends associated with climate change and other anthropogenic perturbations might be detected. Commonly separated by intervals of at least two to four months, these surveys lack the temporal resolution needed to examine any variability in water masses and volume transport that occur on weekly time scales. Furthermore, the spacing of casts (approximately 10 to 20 km) is such that ship surveys also lack the spatial resolution to examine any variability that occurs on small (e.g. 1 km) spatial scales (e.g. Sheehan et al., 2017). Where moorings have been deployed to study the inflows, temporal resolution is high (typically 30 min) (Turrell et al., 1992), but the distance between moorings is greater than that between ship casts (e.g. Turrell et al., 1992). Here, we use observations collected by an autonomous ocean glider to examine water mass characteristics in the northwestern inflows at high temporal and at unprecedented spatial resolution over a two-month period, presenting the most high-resolution description yet of the water masses flowing into the northwestern North Sea. We examine velocity estimates obtained by the glider and estimate the thermohaline (i.e. density-driven) and absolute volume transport of the inflows.

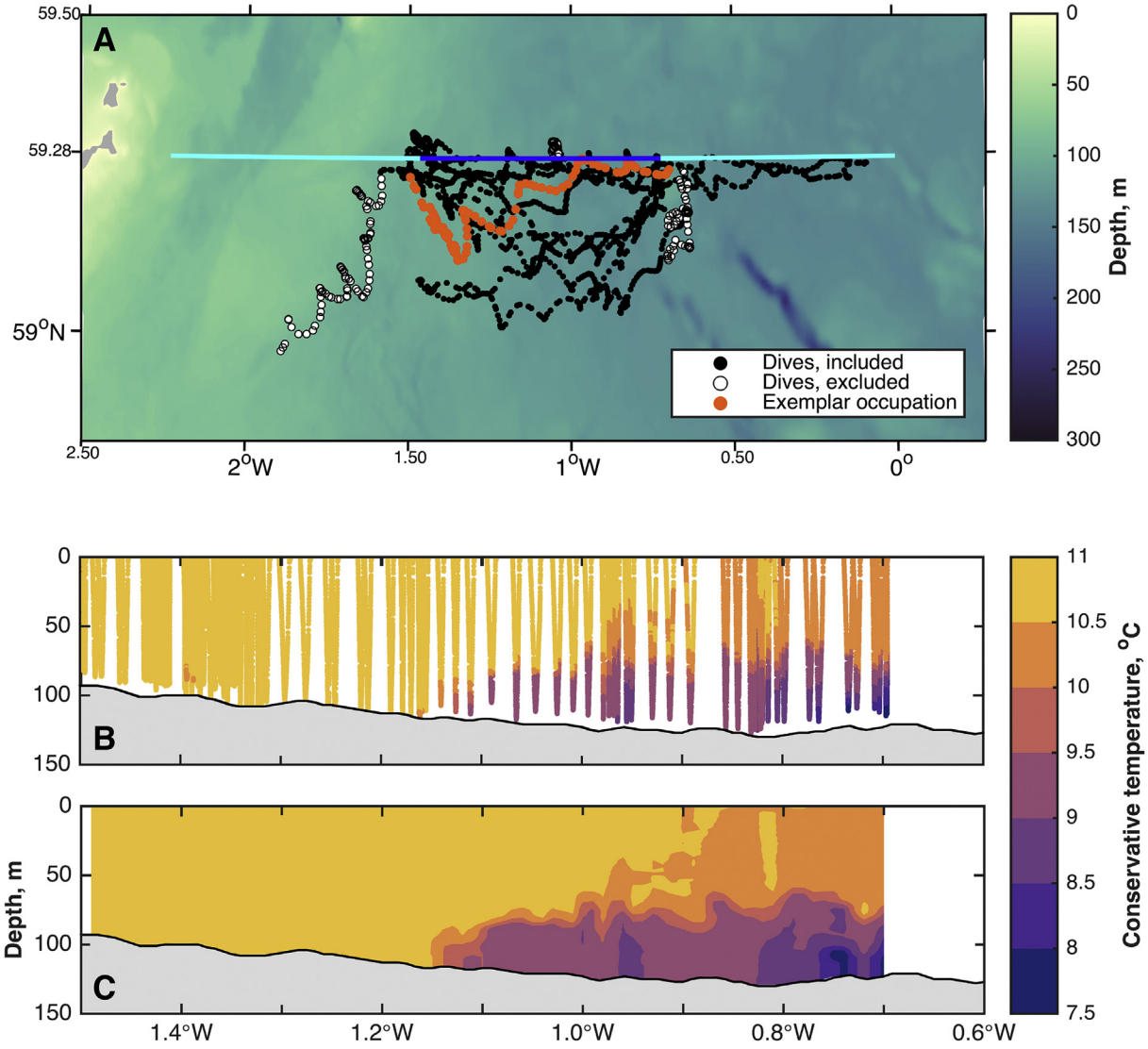

Fig. 2. A. The location of glider dives. Filled black circles indicate dives included in the optimal interpolation; white circles indicate dives excluded from the optimal interpolation. Dives in the exemplar section shown in panel B are shown in orange. Land is shaded grey and the JONSIS line is shown in red. See Fig. 1 for context within the wider North Sea region. B. Glider observations of conservative temperature (°C) from an exemplar section prior to interpolation and C. after interpolation. Note that panel C shows the extrapolated version of the interpolated observations that was used when calculating geostrophic shear (Section 2.2).

2. Data sources and methods

The Joint North Sea Information System (JONSIS) line is a 127 km-long zonal hydrographic section between 2.23°W and the prime meridian at 59.28°N (Fig. 1; Turrell et al., 1996). The line is occupied multiple times a year by Norwegian and British research ships and has been for over 30 years (Sheehan et al., 2017). A Seaglider (SG502; Eriksen et al., 2001) deployed in 2013 made 10 repeat partial sections (Fig. 2) between 12th October and 2nd December (Berx et al., 2018). The glider was deployed during MRV Scotia cruise 1313S (2 to 16 October 2013). 1520 dives (i.e. downcast-upcast pairs) were recovered from the glider; a software fault on the glider resulted in the loss of approximately 1000 dives interspersed throughout the deployment. Dives were, on average, 20 min in duration and 300 m apart.

2.1. Quality control and interpolation

Observations were processed using the UEA Seaglider Toolbox (www.bitbucket.org/bastienqueste/ueaseaglider-toolbox) to optimise the hydrodynamic model of the glider's flight path (Frajka-Williams et al., 2011) and to correct for thermal lag of the un-pumped conductivity cell (Garau et al., 2011). This second process reduces artificial spikes in salinity profiles: erroneous measurements that arise from a mismatch between the water temperature recorded by the glider and the water temperature inside the conductivity cell. The strength of the thermocline in the study region (up to 0.4°C m^{-1}) was such that thermal lag correction alone was insufficient to remove all the spikes (Fig. 3). To remove remaining spikes that were symmetrical about the mean profile of each downcast-upcast pair, salinity observations at a given depth that differed from the mean salinity at that same depth by more than 0.01 g kg^{-1} were removed. The resulting gaps were filled by linear interpolation in the vertical. To remove spikes that were not symmetrical about the mean of an downcast-upcast pair, all salinity casts were then smoothed with a 10 m running mean calculated over a square window. These last two steps had little effect at the top and bottom of casts where vertical gradients are small, but removed spikes at the depth of the thermocline where the unprocessed observations were clearly unphysical (Fig. 3); both steps were necessary to fully remove spikes.

Salinity observations from the ship section completed immediately

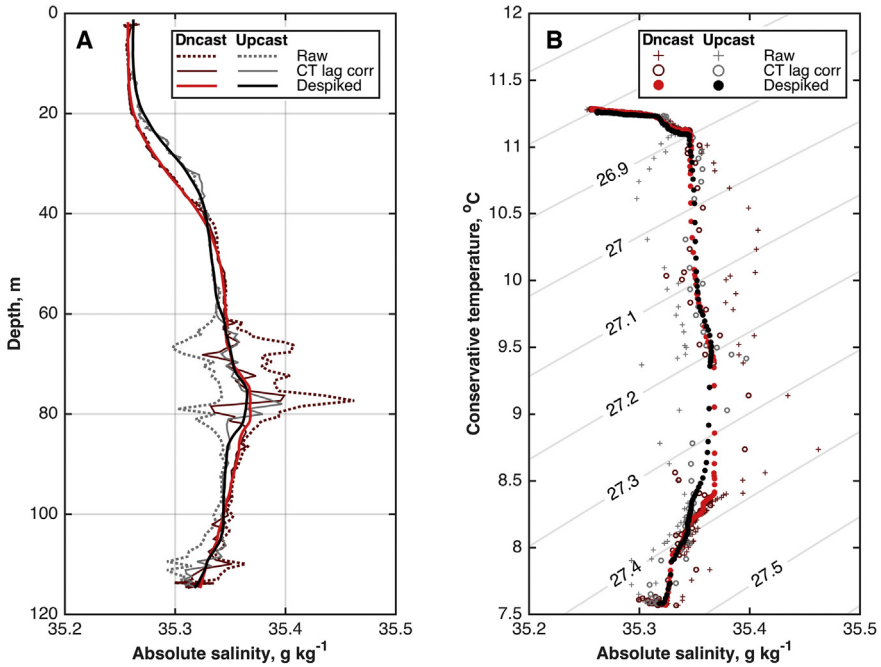

Fig. 3. A. Down- and upcast profiles profiles of absolute salinity (g kg^{-1}) from dive 255 (0.78°W, 17th October 2013, 04:45 UTC) at different stages of the despiking process (see legend). B. The same two profiles plotted in temperature-salinity space, with contours of potential density (grey lines; kg m^{-3}). Dncast: downcast. Raw: uncorrected profile. CT lag corr: profile corrected to minimise effect of thermal lag of the CT cell. Despiked: profile corrected to remove spikes and smoothed with 5 m running median.

after the glider deployment were compared with salinity observations from the first glider section. De-spiked glider salinities from casts closest to the ship stations were interpolated onto the same depths as the ship observations; the median difference was 0.044 g kg^{-1} with a standard deviation of 0.015 g kg^{-1}. This offset was added to the whole time series of glider salinity observations as calibration. Observations from four paired ship-glider profiles were used in this calculation; the profiles were separated in time by between one and three days. A calibration profile contemporaneous with the glider deployment was not available.

Particulate backscatter intensity was calculated from the volume scattering function observed by the glider following the method of Green et al. (2014) and Hall et al. (2017), using a centroid angle of 124° and a wavelength of 470 nm. The wavelength and centroid angle are properties of the instrument. We interpret backscatter intensity as a proxy for suspended sediment concentration. Chlorophyll concentration (not shown) has little influence on backscatter intensity in our observations.

The processed observations were optimally interpolated using a Gaussian weighting function (Bretherton et al., 1976). We assume that the sections are zonal. Observations from pronounced loops in the glider's path due to tidal advection were excluded, as were observations from final dives made by the glider as it travelled south for recovery (Fig. 2a). An exemplar section before and after interpolation is presented in Fig. 2.

2.2. Velocity and transport calculations

Prior to calculating geostrophic shear, the interpolated observations were extrapolated to the seafloor using a nearest-neighbour method where glider observations did not cover the entire water column. 88% of profiles in the interpolated data set were extrapolated; the median extrapolated distance was 9.18 m. The interpolated, extrapolated fields were smoothed horizontally using a Gaussian-weighted running mean. The standard deviation of the Gaussian function was 2 km, the first baroclinic Rossby radius at the latitude of the JONSIS line. Thermohaline velocity – i.e. flow driven by horizontal density gradients – was derived by referencing the geostrophic shear to an assumed level-of-no-motion at the deepest common level between adjacent grid points. Negative velocities are southward.

Estimates of barotropic tidal velocity at the time and location of each glider dive were obtained from the European shelf solution of the TPXO inverse tide model (volkov.oce.orst.edu/tides; 1/30° resolution; Egbert et al., 2010). Tidal velocities were subtracted from dive-average current (DAC) observations. The de-tided DAC velocities were linearly interpolated onto the same longitudinal grid as the hydrographic observations and were smoothed using a horizontal Gaussian-weighted running mean with a radius of 2 km. To estimate the absolute velocity profile, the shear profile was referenced to the DAC: that is, the shear profile was adjusted by a depth-constant value so that its mean equals the de-tided, gridded, smoothed meridional DAC velocity.

Thermohaline transport and absolute transport were derived by vertical and horizontal integration of the thermohaline velocity and absolute velocity respectively. We calculate both the thermohaline transport and the absolute transport over the full width of each glider section; we call this the full-width transport. These transports cannot be compared over time because the width of consecutive glider sections is inconsistent. To enable comparison of transport over time, we calculate thermohaline and absolute transport across that portion of the JONSIS line that is common to all 10 glider sections (Fig. 2A). This 81 km-wide subsection is referred to as the standardised section and the associated transports as the standardised transports.

We follow the method of Naveira Garabato et al. (2002) to estimate transport error arising from uncertainty in the DAC estimates. For each section, we create a set of 1000 assumed errors randomly sampled from a normal distribution with a standard deviation of 4 cm s^{-1}, a representative uncertainty of DACs. The assumed errors are added to the gridded DAC observations, and for each of the 1000 sets the absolute transport is calculated. The standard deviation of these 1000 transports is taken to be the representative uncertainty in absolute transport arising from the DACs.

2.3. Additional data sets

In Section 4, we compare the glider observations to SST maps and model output. Satellite SST observations were obtained from NASA's Multi-scale Ultra-high Resolution Sea Surface Temperature Analysis product (podaac.jpl.nasa.gov/Multi-scale_Ultra-high_Resolution_MUR-SST; Chin et al., 2017). The product is provided at 1/100° resolution and combines observations from multiple sources and interpolates over

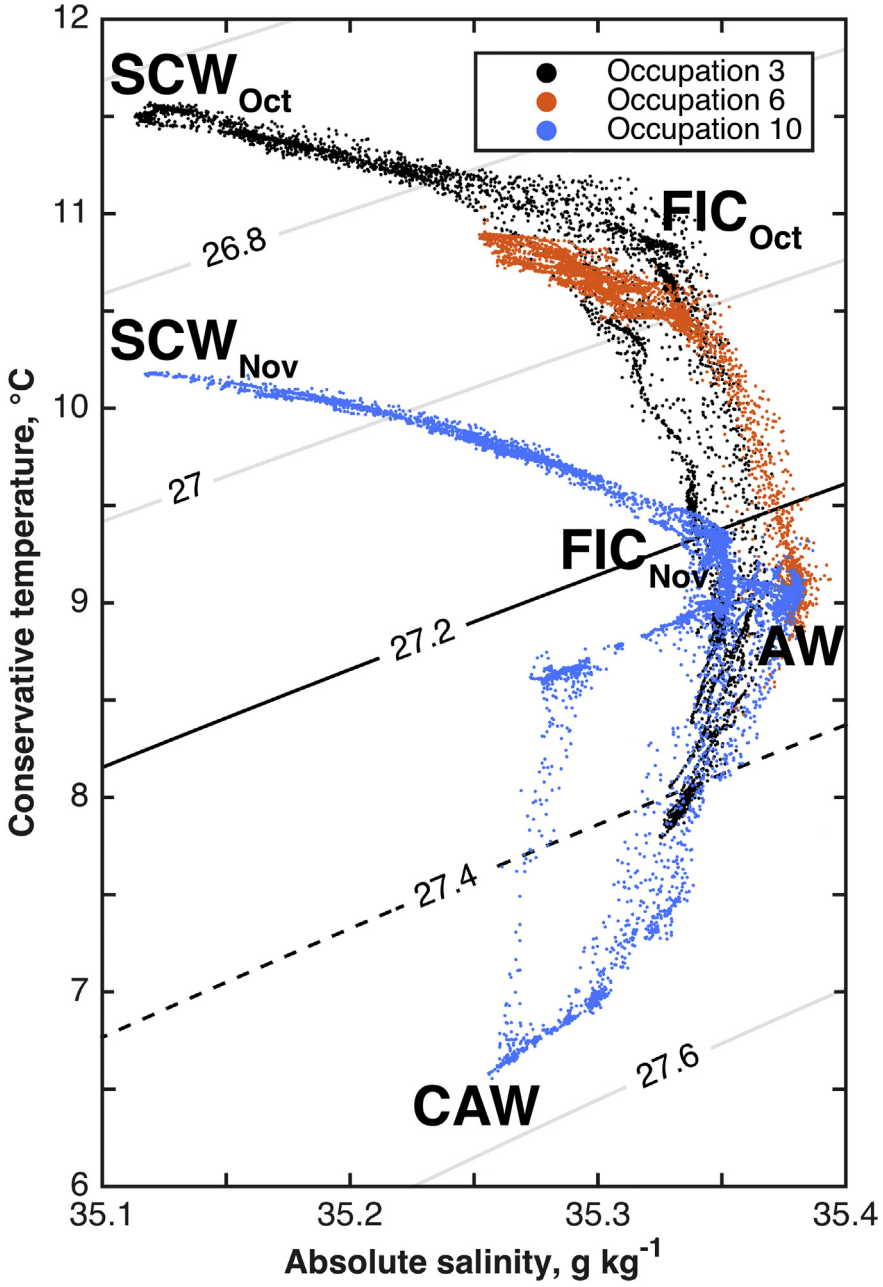

Fig. 4. Temperature-salinity plot of interpolated observations from three sections to illustrate key features of interest: section three (black), six (orange) and 10 (blue). Contours indicate potential density (kg m^{-3}). The 27.2 and 27.4 kg m^{-3} isopycnals are plotted as a solid and dashed black line respectively, as in Figs. 5 and 7. SCW: Scottish Coastal water. FIC: Fair Isle Current water. AW: Atlantic Water. CAW: Cooled Atlantic Water.

gaps arising from, for instance, cloud cover. Model output was obtained from a hindcast run of the UK Met Office's Atlantic Margin Model at 1.5 km resolution (hereafter AMM15; Graham et al., 2018), covering October and November of 2013. The hindcast was not constrained by observations. AMM15 is output on a terrain-following, equal-distance (i.e. points are irregularly spaced in depth, latitude and longitude) grid. Output was linearly interpolated, first onto constant depth levels, then onto a constant longitude grid at the latitude of the JONSIS line (Fig. 2A): the same as was done for the interpolated glider observations. Thermohaline velocity referenced to the deepest common level between adjacent grid points, and thermohaline transport through the standardised section were calculated using the model output following the same method as described above for the glider observations.

3. Results

3.1. Hydrography

Four water masses are observed at the JONSIS line (Figs. 4 and 5). The warmest (11.5°C) and freshest (> 35.2 g kg^{-1}) is Scottish Coastal Water (SCW; Fig. 4; Turrell et al., 1992), which generally occupies the shallower western portion of the section closest to the coast (Fig. 5). The location of SCW is variable on short (four to five days) time scales, which was not apparent in previous ship-based surveys of the region (e.g. Sheehan et al., 2017; Turrell et al., 1992). In sections one to three, SCW extends eastward across the surface, overlying considerably more saline waters immediately below. In section three, a core of SCW is observed at the surface at approximately 1°W (Fig. 5). In section four, some four days later (Table 1), there is no evidence of this core and the

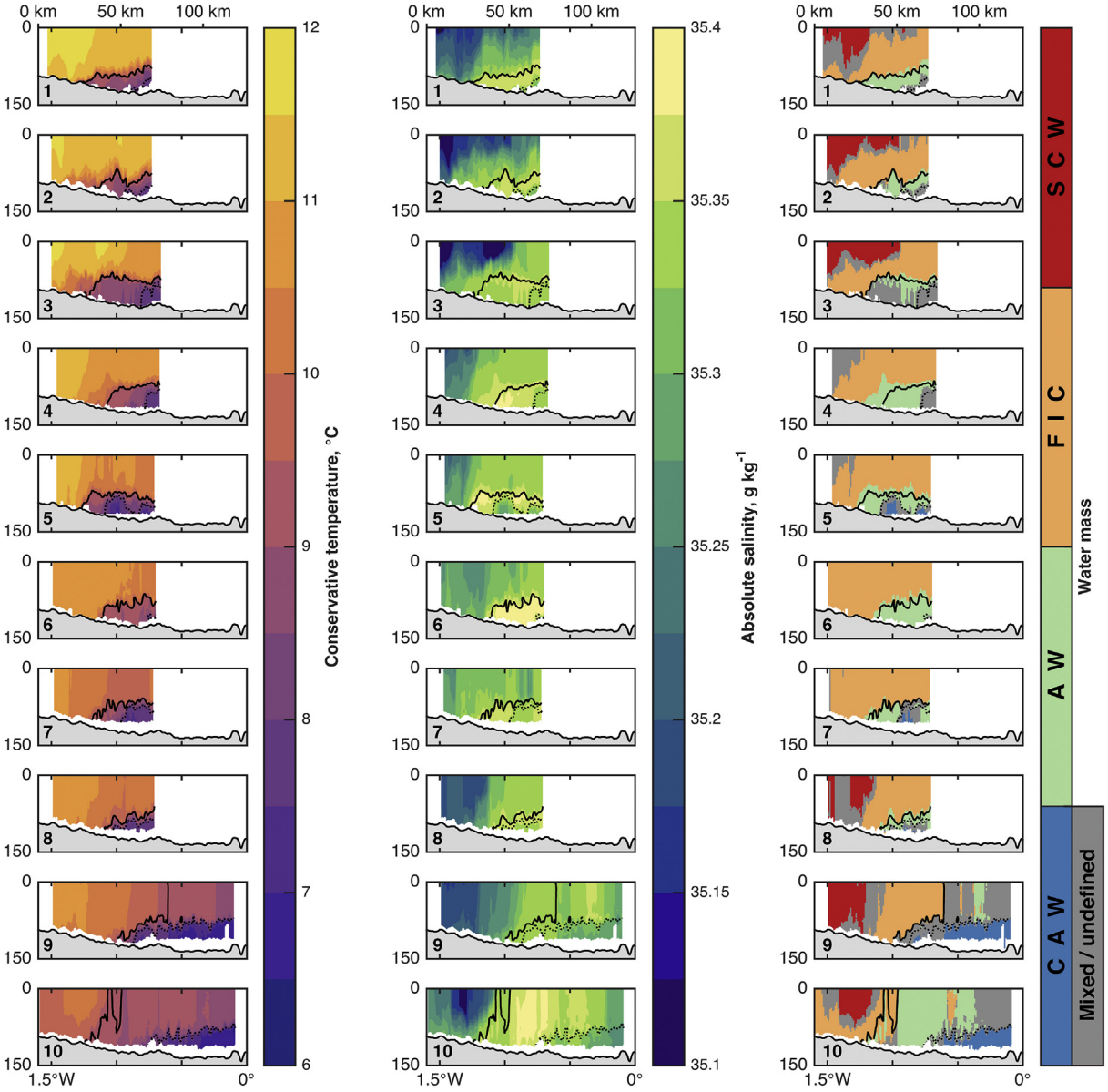

Fig. 5. Interpolated conservative temperature (°C, left), absolute salinity (g kg^{-1}, centre) and water mass distribution (right). Water mass definitions are given in Table 2. The 27.2 kg m^{-3} isopycnal (solid line) and 27.4 kg m^{-3} isopycnal (dotted line) are plotted. Section number is in the bottom left of each panel.

Table 1
Start and finish times of each glider section, and of the whole deployment.

Section number	Start	Finish
Deployment	12 October	
01	14 October	17 October
02	17 October	20 October
03	20 October	25 October
04	25 October	28 October
05	28 October	2 November
06	2 November	5 November
07	5 November	9 November
08	9 November	11 November
09	11 November	19 November
10	19 November	28 November
Recovery		2 December

vertical salinity gradient (not shown) is greatly reduced. In sections four, five, six and seven, SCW is not observed, presumably because it has retreated to shallow, western waters not sampled by the glider. During the two months of the glider deployment, SCW cools by approximately 1.5°C (Fig. 5); this is likely a consequence of surface heat loss over the period. In Fig. 4, we distinguish between the temperature-salinity signal of SCW in October (SCW_{Oct}) and SCW in November (SCW_{Nov}). The cooling increases the density of SCW by almost 0.3 kg m^{-3}. The salinity of SCW remains unchanged over this period.

The water mass that is cooler (11°C) and more saline (35.25 to 35.35 g kg^{-1}; Figs. 4 and 5) than SCW is FIC water, the core water mass of the FIC (Turrell et al., 1992). FIC water is found to the east of SCW and overlies the cooler, more saline waters at the bottom to the east of the section (Fig. 5). In some sections (e.g. five, six and seven), FIC water is present as the previously described well-mixed strip of water, the eastern extent of which overlies more saline water at the seafloor (Turrell et al., 1992, Fig. 5); in other sections (e.g. two and three), this distribution is disrupted by eastward extensions of SCW. From the large number of observations that lie on the mixing line between SCW and FIC water, we infer that a high degree of diapycnal mixing occurs between the two water masses as or before they cross the JONSIS line. We use the same subscript notation as previously to distinguish between the

Table 2
Temperature and salinity criteria used to define water mass distributions in Fig. 5.

Water mass	Temperature (°C)	Salinity (g kg^{-3})
SCW, Scottish Coastal Water		S⩽35.2
FIC water, Fair Isle Current water	T⩾9.25	35.25⩽S < 35.35
AW, Atlantic Water		S⩾35.35
CAW, Cooled Atlantic Water	T⩽7.5	

temperature-salinity signal of FIC water in October and the temperature-salinity signal of FIC water in November. The observed temperature decrease in FIC water matches that of SCW (Fig. 4).

The most saline water observed by the glider (> 35.35 g kg^{-1}; Figs. 4 and 5) is the most undiluted Atlantic-origin water to be found in the northwestern inflows (Turrell et al., 1992); this is known as Atlantic Water (AW). In observations obtained in September 1987, Turrell et al. (1992) find AW at the bottom of the water column, to the immediate east of FIC water. They trace its path northward to the Shetland Islands, where water of the same salinity is found at the surface, and conclude that it subducts under FIC water as it travels southward – see the map presented in their Fig. 7. The observations presented here suggest a more complicated picture. The density of AW lies largely between 27.2 and 27.4 kg m^{-3} (Fig. 4); in the first eight sections, this density range is found beneath the main thermocline. Consequently, AW is observed at the JONSIS line as an often thin (approximately 10 to 50 m) bottom or near-bottom layer, the distribution of which is highly variable (Fig. 5). As the density distribution at the JONSIS line changes with the cooling of the inflows, the 27.2 kg m^{-3} isopycnal outcrops between sections eight and nine; it then retreats shoreward (i.e. westward) between sections nine and ten (Fig. 5). Consequently, AW is able to occupy a greater proportion of the JONSIS line (e.g. section 10) and, furthermore, is able to reach the surface (Fig. 5). This suggests that the subduction of AW beneath lighter SCW and FIC water is likely a summer phenomenon that depends on the degree and duration of stratification.

The coldest (> 7.5°C), densest (> 27.4 kg m^{-3}) water observed by the glider is Cooled Atlantic Water (CAW; Turrell et al., 1992). It is observed only in the deepest and easternmost parts of the section (Fig. 5). CAW is what remains of water trapped beneath the seasonal pycnocline, its temperature being set by ocean-atmosphere exchange the preceding winter (Turrell et al., 1992). CAW is thought to cover large portions of the seafloor in the northern North Sea, and the horizontal density gradients between it and surrounding lighter water masses are a key driver of thermohaline circulation in the region (Hill et al., 2008). Our observations place the limit of CAW at approximately 1°W: further west than was previously thought (Turrell et al., 1992). The salinity of CAW (35.25 g kg^{-1}) is lower than that of AW, and is even slightly lower than that of FIC water (Fig. 4). This is potentially a consequence of fresh water input from rainfall and runoff, and potentially of mixing with SCW, when the water column is well mixed during winter (Turrell et al., 1992).

CAW and AW are the most turbid water masses (Fig. 6). The highest values of backscatter intensity are found, in the first eight sections, at depths below the 27.2 kg m^{-3} isopycnal (Fig. 6); in the final two sections, the highest concentrations are found below the 27.4 kg m^{-3} isopycnal. Low backscatter intensities are found immediately above the pycnocline to the east of the section, and intermediate intensities are found in FIC water and SCW to the west of the section (Fig. 6). If we assume the primary input of sediment comes from the seafloor, and given that depth-mean integrated backscatter intensity is generally fairly constant across the section (Fig. 6), the higher intensities found in CAW and AW arise because the pycnocline traps sediment close to the sea floor. In the west of the section, where mixing is likely stronger (Dooley, 1974; Sheehan et al., 2017), sediment is more evenly distributed throughout the water column (Fig. 6).

3.2. Velocity and transport

Thermohaline velocity across the JONSIS line is focused into four to six narrow, southward-flowing jets with a characteristic width of approximately 10 km (Fig. 7). The fastest of these jets have peak surface velocities in excess of 0.3 m s^{-1}, although the majority have peak surface velocities of between 0.2 and 0.3 m s^{-1}. Most of these jets are southward and are associated with upward tilt of isopycnals towards the east (Fig. 7), which is particularly pronounced where the 27.2 kg m^{-3} isopycnal meets the seafloor. The alternating bands of northward and southward thermohaline flow associated with either domes or depressions in the isopycnals (Fig. 7) indicate the presence of baroclinic eddies.

The absolute velocity is strongly influenced by the addition of barotropic flow that is captured by referencing geostrophic shear to DAC (Figs. 7 and 8). DAC is generally southward (Fig. 8). Maximum absolute velocities are comparable to maximum thermohaline velocities, but the absolute flow occurs in broad zonal bands across the section, rather than being concentrated into narrow jets (Fig. 7). The horizontal structure of absolute velocity changes in time (Fig. 7). In some sections (e.g. three and four), there is southward flow across full width of the section; in other sections (e.g. eight, nine and 10), there are two regions of strong southward flow separated by a region of near-zero flow. This is possibly evidence of the separation of the northwestern inflows, the FIC being the western portion of the inflow and the ESAI being the eastern portion of the inflow, and agrees with current meter observations from further south that indicate the presence of separate southward flows (Turrell et al., 1992). However, the limited widths of the glider sections do not allow us to determine with certainty whether the inflows are sometimes joined and sometimes separate, or whether the inflows are always separate and are moving zonally across the standardised section. We consider this point in the context of models in Section 4.2.

Absolute transport is consistently greater than thermohaline transport during all 10 sections, both when integrated over the full-width of each section and when integrated over the standardised section (Fig. 9). The mean standardised absolute transport is 0.44 Sv (mean uncertainty ± 0.018 Sv); the mean standardised thermohaline transport is 0.14 Sv. The temporal variability of standardised absolute transport (standard deviation 0.13 Sv) is also greater than the temporal variability of standardised thermohaline transport (standard deviation 0.05 Sv). Specific examples of sharp temporal change stand out: for instance, the 0.37 Sv increase in standardised absolute transport between sections two and three, from 0.25 ± 0.018 Sv to 0.62 ± 0.019 Sv. Full-width transport increases from 1.10 ± 0.030 Sv to 1.71 ± 0.031 Sv between sections nine and 10; the two sections are of similar length (78 and 85 km respectively; Fig. 9b). In contrast, thermohaline transport does not exhibit such large short-term variability during the period of the observations. This is likely because the processes that contribute to absolute transport in addition to thermohaline transport – in particular, the wind, the influence of which we do not consider in detail here – vary on shorter time scales than the density gradients that drive thermohaline transport. Estimates of absolute transport across the full width of the JONSIS line are not available, but estimates of thermohaline transport across the full width of the JONSIS line from ship observations are available from the dataset compiled by Sheehan et al. (2017). Two ship sections coincide with the glider deployment, and both suggest that the glider sections captured approximately half of the thermohaline transport (Fig. 9a). This is likely because the glider sections are not capturing the primarily salinity-driven thermohaline transport that occurs west of 1.5°W during autumn (Sheehan et al., 2017).

Transport uncertainties arising from uncertainty in DAC observations are between one and two orders of magnitude smaller than the transports themselves and the error bars of consecutive sections do not overlap (Fig. 9a). The principal limitation of the transport estimates

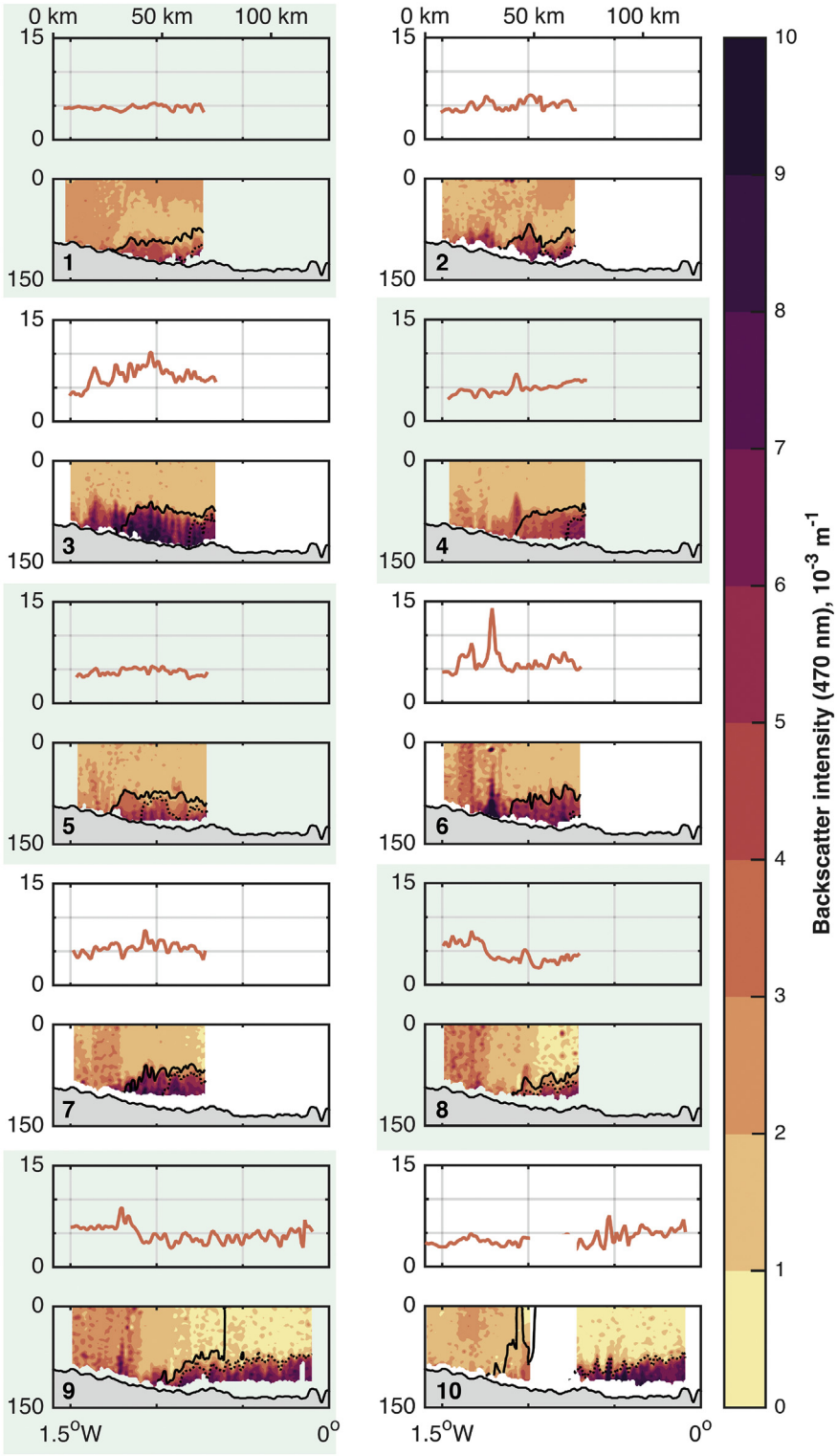

Fig. 6. Interpolated backscatter intensity (contour plots, bottom of each pair; 10^{-3} m^{-1}) and depth-mean integrated backscatter intensity (line plots, top of each pair; 10^{-3} m^{-1}). The 27.2 kg m^{-3} isopycnal (solid line) and 27.4 kg m^{-3} isopycnal (dotted line) are plotted, and section number is in the bottom left of each panel pair.

presented above is the limited width of the standardised section, which is clearly capturing only a part of the transport across the JONSIS line and of the inflows, both thermohaline and absolute (Fig. 9).

4. Discussion

4.1. Atlantic Water

The full-depth spreading of AW observed during the final glider section (Fig. 5) is likely the first phase in the formation of CAW for the

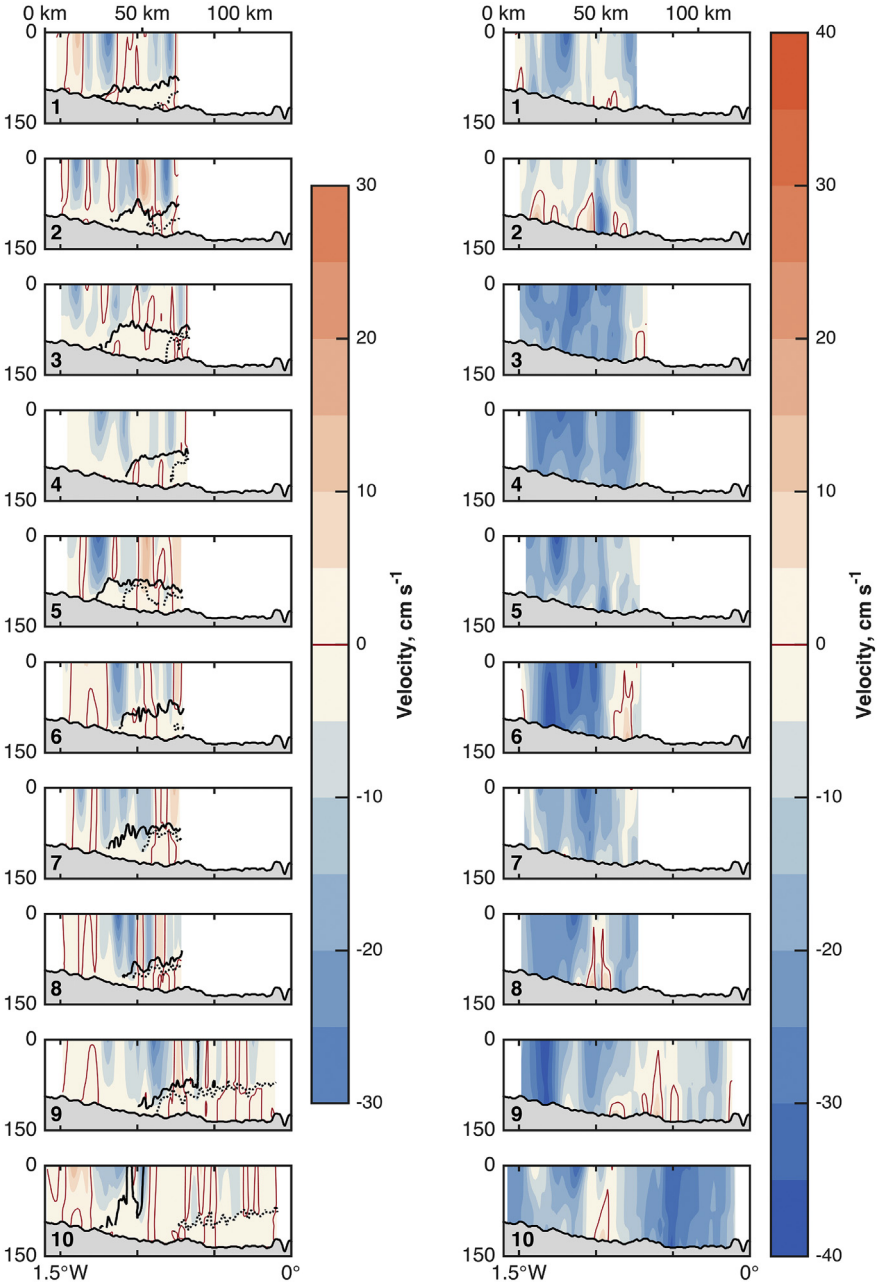

Fig. 7. Meridional thermohaline (left) and absolute (right) velocity (m s^{-1}). Negative velocities are southward. Tidal flows have been extracted. The 27.2 kg m^{-3} isopycnal (solid line) and 27.4 kg m^{-3} isopycnal (dotted line) are plotted (left panels only). The zero contour is indicated by the dark red line. Section number is in the bottom left of each panel.

following year, bringing AW into contact with the atmosphere until the formation of the next year's seasonal pycnocline submerges it below warmer surface layers. AW entering the North Sea via the northwestern inflows, particularly at times of year when it is in contact with the atmosphere is therefore a key means by which open-ocean properties may propagate into and be stored in the interior of the North Sea on interseasonal time scales. Furthermore, the properties of AW entering the North Sea in autumn and winter, before its conversion to CAW, could therefore be of key importance to bottom-dwelling organisms, as these properties will set the hydrographic conditions of benthic habitats for the coming year.

4.2. Frontal jets and eddies

Frontal jets associated with the bottom front between FIC water and CAW are a well-known feature of the northwestern inflows (Dooley, 1974; Sheehan et al., 2017, 2018; Turrell, 1992) and have been observed elsewhere in the North Sea (e.g. Brown et al., 1999); but the presence of multiple narrow jets is as yet undocumented. Multiple narrow jets are not apparent in thermohaline velocity sections derived from long-term, low-resolution ship observations, either when considered as seasonal means (Sheehan et al., 2017) or as individual sections (not shown); neither has their width been determined from studies of current meter observations (e.g. Turrell et al., 1990). In the southern North Sea, frontal jets approximately 15 km in width have been observed in the region of Dogger Bank (Fig. 1; Brown et al., 1999). These jets, slower than those reported here, were observed to border a cold pool of water lying below the thermocline between Dogger Bank and the eastern coast of the United Kingdom (Brown et al., 1999), a hydrographic setting that resembles the bottom boundary between FIC

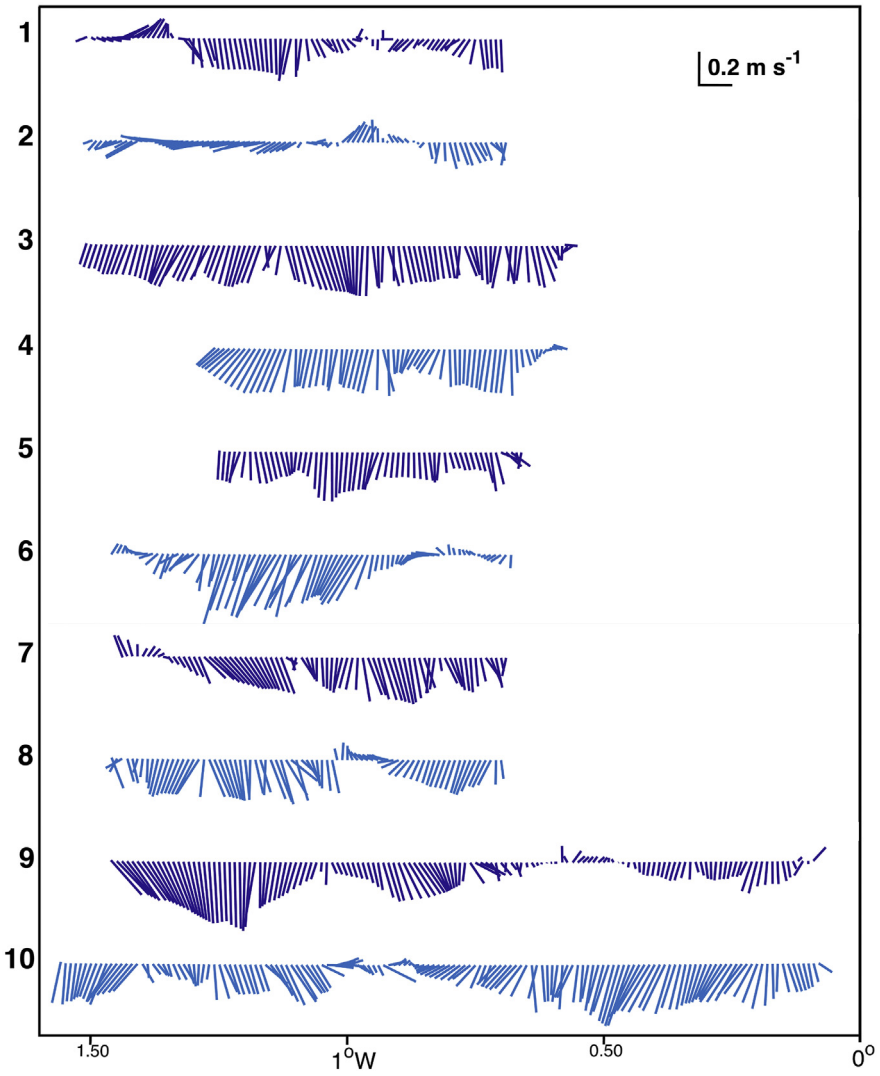

Fig. 8. DAC observations, de-tided, projected onto the JONSIS line along meridians and gridded by section. Transect number is on the left-hand side.

water and CAW observed in this study (Fig. 5).

The presence of multiple thermohaline jets associated with the same frontal system appears to be a new finding for the North Sea as does the week-to-week variability in the strength, location and number of the jets (Fig. 7). We speculate that this is because the frontal system associated with the northwestern inflows has multiple causes, being in part a tidal mixing front and in part a boundary between different water masses advected to the region from elsewhere (Sheehan et al., 2018). The interplay between these different processes of frontal formation leads to horizontal density gradients that are more complex and more variable than would be the case were the front a classic tidal mixing front. The presence of these narrow jets, and the presence of eddies, have implications for the transport of tracers, including pollutants, and organisms at times of year – i.e. summer – when thermohaline flow dominates in the northwestern inflows: transport pathways may be more locally variable than if a single, broader thermohaline flow were present.

To our knowledge, baroclinic eddies in the northwestern inflows have not previously been observed, and likely for the same reason that the multiple narrow jets have not previously been observed: prior observations lacked the sub-kilometre spatial resolution made possible by gliders. Badin et al. (2009) propose that geostrophic eddies in shelf seas may be generated at frontal boundaries by baroclinic instability during periods when stratification is present. The presence of stratification and baroclinic jets (Fig. 7) suggests that the frontal baroclinic instability hypothesis of shelf sea eddy formation is applicable to the northwestern inflows. Many previous studies have examined tidal mixing in the region (e.g. Sheehan et al., 2018; Svendsen et al., 1991; Turrell et al., 1996), but these eddies may be an unappreciated method by which mixing of different water masses in the northwestern inflows is achieved (Badin et al., 2009). For example, instances of eastward deviation of SCW in sections one and 10 appear to be associated with eddies (Figs. 5 and 7).

Neither the jets nor the eddies are visible in maps of sea surface temperature (Fig. 10, top panels). Near-circular features in SST such as are apparent during sections two, four and six could be interpreted as eddies, but no baroclinic eddy visible in the thermohaline velocity sections appears to have an SST signature (Figs. 5 and 10, top panels). Thermohaline jets also lack an obvious SST signature (Fig. 10, top panels), potentially because the structure of the thermohaline jets is often obscured by barotropic flow, which is frequently observed to be the dominant component of the overall velocity distribution (Fig. 7). The SST distribution does show the relatively gradual transition between warm SCW waters in the west and cooler FIC water – and, latterly, AW (section 10; Fig. 5) – in the east (Fig. 10, top panels), and the zonal movement of, for instance, the 11.5°C isotherm during the first five sections is a good indication of short-term variability in the distribution of SCW identified in the glider observations. However, it is the bottom

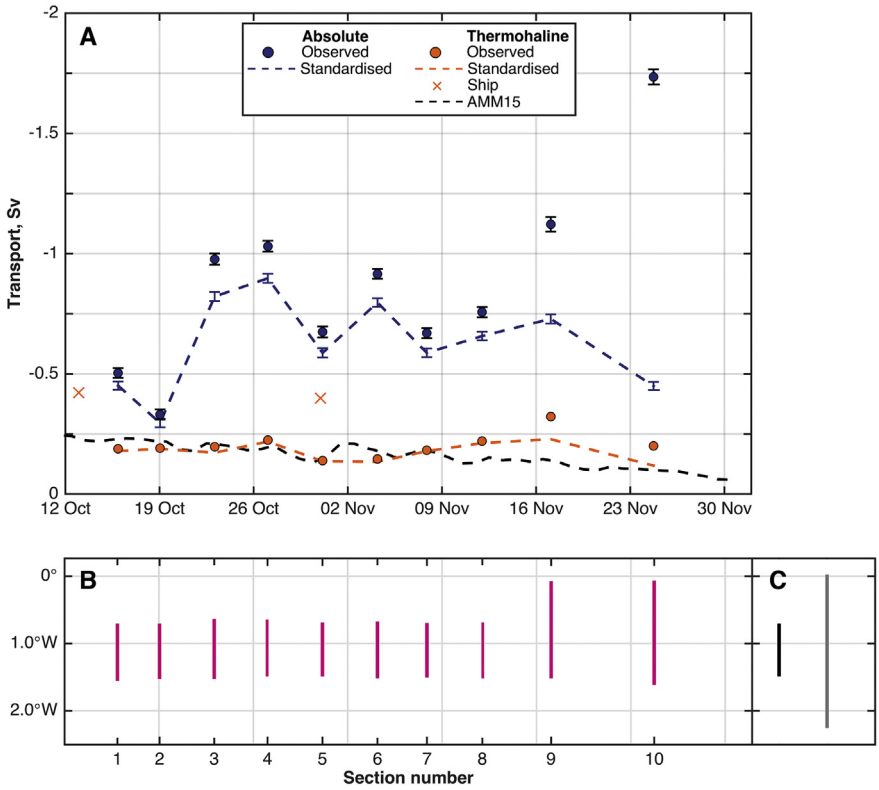

Fig. 9. A. Absolute (blue) and thermohaline (orange) volume transport (Sv). Circles indicate full-width transport in each section; dashed lines indicate transport across the standardised section; crosses indicate thermohaline transport from ship-based observations of the full, 127 km JONSIS line (Sheehan et al., 2017). Error bars indicate ± one standard deviation, derived from Monte Carlo error estimation (Section 2). Dashed black line indicates thermohaline transport through the standardised section from AMM15. Note that the *y* axis has been reversed. B. Pink lines indicate the portion of the JONSIS line sampled by the glider in each section (pink lines). C. The standardised section: the part of the JONSIS line sampled by the glider in all 10 sections (black line) and the full JONSIS line (grey line).

front, rather than surface fronts, that is the primary dynamical driver of the frontal system (Hill et al., 2008; Sheehan et al., 2017; Turrell et al., 1992). The SST maps conceal key dynamical features of the northwestern inflows, further demonstrating the importance of sharp bottom fronts in shelf sea systems and highlighting the need for validating models against high-resolution, full depth observations as can be made by gliders.

Thermohaline frontal jets are visible in the AMM15 hindcast simulation (Fig. 11), although they are broader and slower than in the observations (Fig. 7), having a characteristic width of between 10 and 20 km and maximum speeds of approximately 20 cm s^{-1}. A comparison of absolute surface velocity maps (Fig. 10, bottom panels) and thermohaline velocity sections (Fig. 11) demonstrates that absolute surface velocity cannot be the result of thermohaline processes alone, in agreement with the glider observations (Fig. 7). Peak absolute surface velocities (40 cm s^{-1}) are approximately double peak thermohaline surface velocities (20 cm s^{-1}), and surface flows are far broader than the narrow thermohaline jets, even as they appear in AMM15 (Fig. 11). We speculate that this fast, broad flow is primarily wind-driven. A full discussion of wind forcing of the northwestern inflows is outside the scope of this study, but it appears that wind-driven flow switches between the FIC (from the northwest; Fig. 1) and the ESAI (from the north-northeast; Fig. 1) during the period of the glider observations (Fig. 10, bottom panels), perhaps as atmospheric circulation patterns favour flow in one current over the other. When wind flow in the FIC is strong, there is a bifurcation of the current around Fair Isle that sometimes persists as far south as the JONSIS line, and sometimes further south still (Fig. 10, bottom panels). This could be the cause of the interstitial regions of near-zero absolute velocity in the glider observations (Fig. 7), rather than a separation of the FIC and ESAI (Section 3.2; Turrell et al., 1992).

In the absence of an apparently wind-driven flow, what appear to be thermohaline jets dominate the inflows (Fig. 10, bottom panels; section 1), which is expected when wind forcing is minimal (Turrell, 1992; Turrell et al., 1990). We note that a southward-flowing surface jet crossing the JONSIS line to the immediate west of 1°W is visible in the surface velocity map (Fig. 10) and in the thermohaline velocity section (Fig. 11) and is of comparable speed (15 to 20 cm s^{-1}) in both. These jets originate to the north in the Fair Isle Gap – i.e. between the Shetland and Orkney archipelagoes – and thus are capable of supporting inflow to the North Sea when wind flow is weak.

There is no evidence in the model of baroclinic eddies in the region covered by the glider sections, and there are no undulations in the 27.2 and 27.4 kg m^{-3} isopycnals (Fig. 11). Some eddies are visible in the model, but they are further west (approximately 1.7°W; not shown). They are associated with the salinity front between SCW and FIC water, and not with the hydrographically complex bottom temperature front that is the primary driver of both frontal and eddy dynamics in the glider observations.

4.3. Transport

The mean absolute transport estimates reported here are higher than those reported by Turrell et al. (1990) based on mooring observations (30-minute temporal resolution) from the autumn of 1987 at seven locations across the northwestern inflows further south in the North Sea. They report mean absolute transports of 0.37 and 0.39 Sv for October and November respectively. The absolute transport of 1.71 Sv observed during section 10 is greater than any single value reported by Turrell et al. (1990). Their 89 km-wide section was almost three times wider than the standardised section used here, and given that our standardised section is not capturing a considerable amount of transport in the FIC and ESAI, the transport of the inflows during the observations of Turrell et al. (1990) would appear to be lower than during our campaign. Turrell et al. (1990) report a standard deviation of transport of 0.29 and 0.28 Sv for October and November respectively. This variability is greater than that reported here, but the high temporal resolution of their mooring observations (30 min) would capture greater variability than the glider observations.

Transport estimates are also available from models. Winther and Johannessen (2006) model the circulation of the North Sea over a year; they estimate a mean absolute volume transport of 0.50 Sv for the FIC

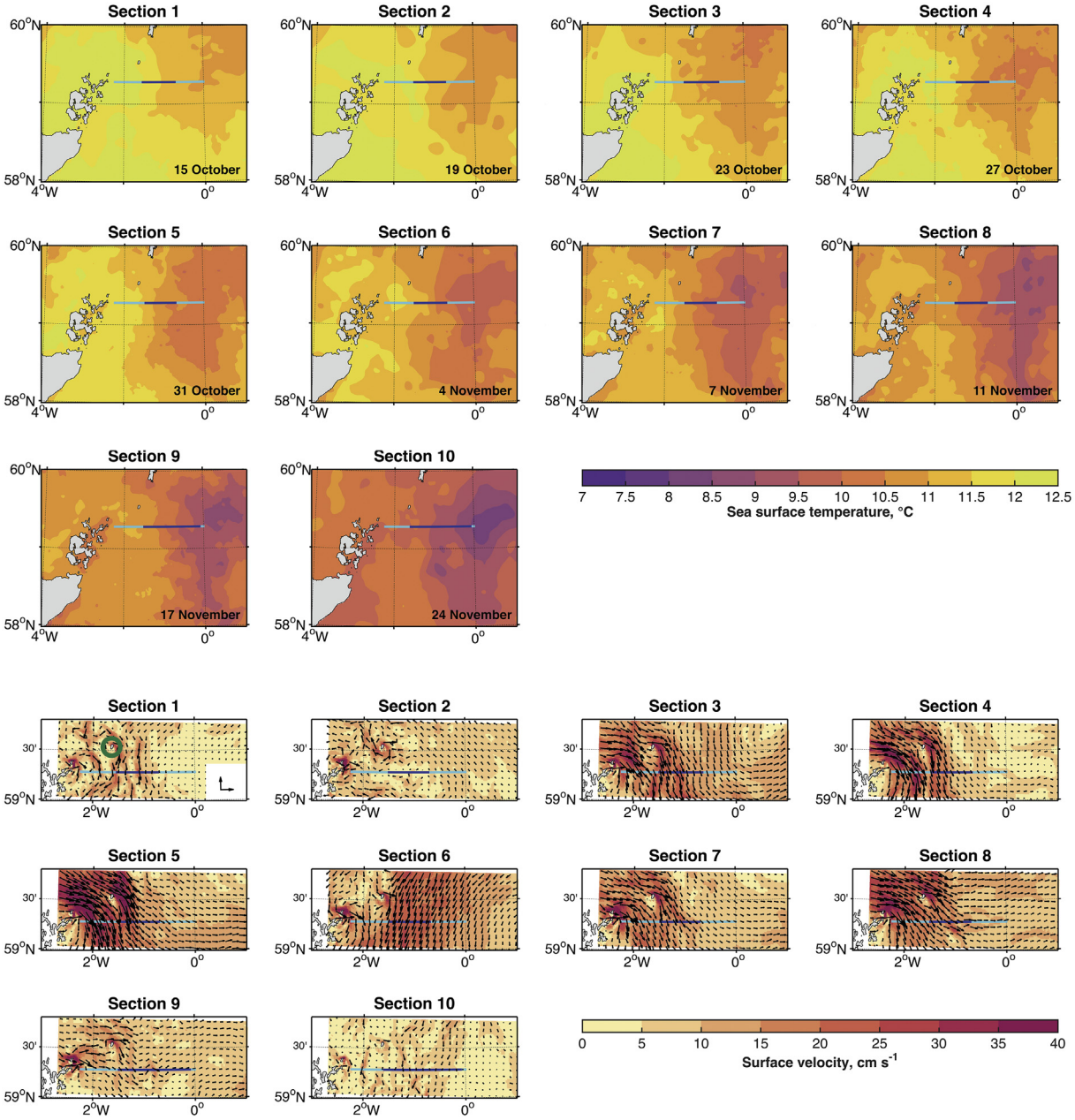

Fig. 10. Top 10 panels. Daily-mean SST maps (°C) of the middle day of each glider section. The width of each partial section (dark blue) is plotted relative to the width of the JONSIS line (light blue). The date of each map is in the bottom right-hand corner. Note that, although the colour bar limits are different, the colours of each contour interval match those in Fig. 5. Bottom 10 panels. Daily mean surface velocity (vectors; m s^{-1}; every fifth grid point is plotted for clarity) and speed (m s^{-1}) maps from AMM15. The key plotted in section 1 shows arrows of 25 cm s^{-1}. The location of Fair Isle is indicated by the green circle in section 1. The days plotted are the same as in the top panels.

and 0.49 Sv for the ESAI, giving a combined transport of 0.99 Sv for the northwestern inflows within the North Sea. Again, the limited width of the standardised section makes a direct comparison with our estimates difficult, but the estimates of Winther and Johannessen (2006) are of a similar magnitude to glider estimates of transport integrated over the full width of each section (Fig. 9). Between October and December, Holt and Proctor (2008) estimate mean absolute transport of the FIC through the Fair Isle Gap to be 0.56 and 0.47 Sv from simulations at different resolutions. These estimates exclude the ESAI, and are higher than at other times of year. Considering the limited width of our standardised section and the addition of the ESAI in our estimates, the estimates of Holt and Proctor (2008) would not appear to be substantially different from our own. A more recent and direct comparison may be made with AMM15. Thermohaline transport in the AMM15 hindcast through the standardised section compares favourably with observational estimates from the glider, particularly during October, both in terms of magnitude and variability (Fig. 9). The lack of northward flow associated with the eddies and the broader width of the jets would appear to compensate for the reduced velocity of the jets when integrating to estimate transport.

5. Conclusion

Observations from a two-month glider deployment along the JONSIS line in the autumn of 2013 have been analysed to describe the hydrographic properties and volume transport of the FIC and ESAI, the northwestern inflows to the northern North Sea, at high spatial and temporal resolution. Horizontal temperature and salinity gradients

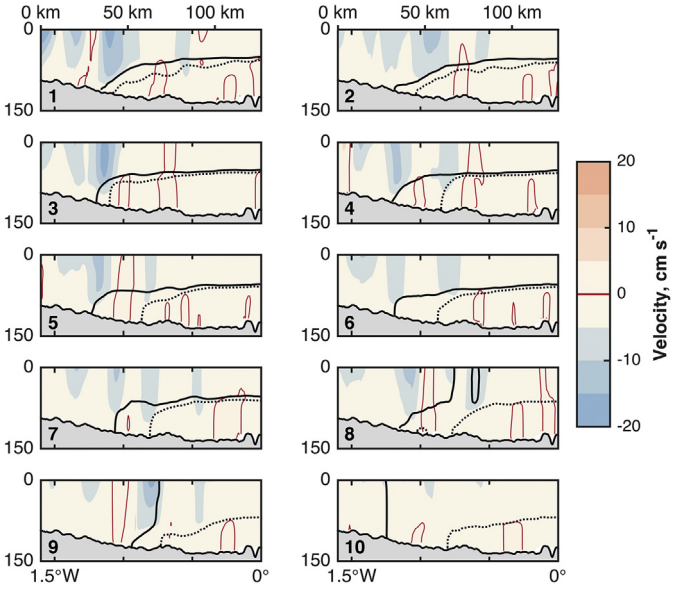

Fig. 11. Daily-mean thermohaline velocity of the middle day of each glider section from AMM15. The days plotted are the same as in Fig. 10. Negative velocities are southward. The 27.2 kg m^{-3} isopycnal (solid line) and 27.4 kg m^{-3} isopycnal (dotted line) are plotted. The zero contour is indicated by the dark red line. Section number is in the bottom left of each panel. Note that, although the colour bar limits are different, the colours of each contour interval match those in Fig. 7.

across the section give rise to southward thermohaline jets and which tend to be associated with the eastward-upward tilt of the isopycnals over AW and CAW intrusions. Our observations place the westward limit of CAW at approximately 1°W, further west than it has previously been observed. Thermohaline flow is appreciable even as stratification decays during autumn. Baroclinic eddies, not previously observed in the region, are visible in the thermohaline velocity distribution. The existence of thermohaline flow in the northwestern inflows has been long established (e.g. Dooley, 1974; Hill et al., 2008; Turrell, 1992; Turrell et al., 1992), but whereas previous studies have identified fairly broad thermohaline jets of some 50 to 70 km across (e.g. Sheehan et al., 2017), our results reveal the presence of multiple narrow jets with widths of approximately 10 km. Previous studies have lacked sufficient spatial resolution to separate individual thermohaline jets. Volume transport in the northwestern inflows is dominated by the barotropic component. The maximum velocities of thermohaline and non-thermohaline flow are comparable: the dominance of the latter comes instead from the broad spatial scales of non-thermohaline flow relative to the narrow thermohaline jets. The limited width of the glider-occupied section means that glider observations of transport do not capture the entire flow of the inflows.

The weekly variability, both spatial and temporal, in the hydrography and transport of the northwestern inflows described here have not been described in previous studies of the northwestern inflows (e.g. Sheehan et al., 2017; Turrell et al., 1992). The region hosts diverse and markedly different water masses of distinct coastal and oceanic origin. We show that the distribution of key water masses changes on weekly time scales and responds quickly to changes in the density distribution brought about by the decay of seasonal stratification. The velocity distribution responds to these changes. The evidence of variability presented here adds to the difficulty of managing and limiting the influence of human activity on the North Sea. Future assessments of the northern North Sea and of the northwestern inflows should account for this variability when attempting to define a background state against which future changes may be assessed. Future modelling efforts should represent the spatial and temporal variability that we have identified.

Author contributions

PMFS carried out the research and prepared this paper. BB, AG, RAH, KJH and BYQ supported the research and provided feedback on earlier drafts of the paper. BYQ assisted with the glider data processing.

Declaration of competing interest

The authors declare that they have no competing interests.

Acknowledgements

PMFS was funded by NERC CASE PhD studentship NE/L009242/1 awarded to UEA and Marine Scotland Science. Seaglider 502 was owned and maintained by the UEA Marine Support Facility. We thank Gillian Damerell and the scientists and crew of the MRV Scotia for deploying the glider, and the crew of the MPV Jura for recovering the glider. We are grateful for the financial support from NERC for the deployment as a demonstration for UK-IMON. The deployment was part of the Brahan project (www.thebrahanproject.com). The glider data presented in this paper are archived at the British Oceanographic Data Centre (doi.org/10/ck8r; Berx et al., 2018). We are grateful to Jennifer Graham for providing access to AMM15 hindcast simulation. We thank the two anonymous reviewers for their gratefully received suggestions for improving the original draft of this paper.

References

Badin, G., Williams, R.G., Holt, J.T., Fernand, L.J., 2009. Are mesoscale eddies in shelf seas formed by baroclinic instability of tidal fronts? J. Geophys. Res. 114, C10021.
Beaugrand, G., 2004. The North Sea regime shift: evidence, causes, mechanisms and consequences. Prog. Oceanogr. 60, 245–262.
Berx, B., Damerell, G.M., Gallego, A., Hall, R.A., Heywood, K.J., Lee, G.A., Queste, B., 2018. Glider Observations of Northwestern Inflows of Atlantic Water to the North Sea. 10/ck8r.
Bretherton, F.P., Davis, R.E., Fandry, C.B., 1976. A technique for objective analysis and design of oceanographic experiments applied to Mode-73. Deep-Sea Res. 23, 559–582.
Brown, J., Hill, A.E., Fernand, L., Horsburgh, K.J., 1999. Observations of a seasonal jet-like circulation at the central North Sea cold pool margin. Estuar. Coast. Shelf Sci. 48, 343–355.
Chin, T.M., Vazquez-Cuervo, J., Armstrong, E.M., 2017. A multi-scale, high-resolution analysis of global sea-surface temperature. Remote Sens. Environ. 200, 154–169.
Dickson, R.R., Meincke, J., Malmberg, S.A., Lee, A.J., 1988. The great salinity anomaly in the northern North Atlantic 1968–1982. Prog. Oceanogr. 20, 103–151.
Dooley, H.D., 1974. Hypotheses concerning the circulation of the northern North Sea. J. Cons. Int. Explor. Mer 36, 54–61.
du Bois, P.B., 1996. Mapping of water masses in the North Sea using radioactive tracers. Endeavour 20, 2–7.
Edwards, M., Beaugrand, G., Reid, P.C., Rowden, A.A., Jones, M.B., 2002. Ocean climate anomalies and the ecology of the North Sea. Mar. Ecol. Prog. Ser. 239, 1–10.
Egbert, G.D., Erofeeva, S.Y., Ray, R.D., 2010. Assimilation of altimetry data for nonlinear shallow-water tides: quarter-diurnal tides of the northwest European shelf. Cont. Shelf Res. 30, 668–679.
Emeis, K.C., van Beusekom, J., Callies, U., Ebinghaus, R., Kannen, A., Kraus, G., Kröncke, I., Lenhart, H.J., Lorkowski, I., Matthias, V., Möllmann, C., Pätsch, J., Scharfe, M., Thomas, H., Weisse, R., Zorita, E., 2015. The North Sea: a shelf sea in the anthropocene. J. Mar. Syst. 141, 18–33.
Eriksen, C.C., James Osse, T., Light, R.D., Wen, T., Lehman, T., Sabin, P.L., Ballard, J.W., Chiodi, A.M., 2001. Seaglider: a long-range autonomous underwater vehicle for oceanographic research. IEEE J. Ocean. Eng. 26, 424–436.
EU, 2008. Directive 2008/56/EC of the European Parliament and of the Council, 17th June 2008 (Marine Strategy Framework Directive). Off. J. Eur. Union (L164), 19–40.
Frajka-Williams, E., Eriksen, C.C., Rhines, P.B., Harcourt, R.R., 2011. Determining vertical water velocities from Seaglider. J. Atmos. Ocean. Technol. 28, 1641–1656.
Furnes, G.K., Hackett, B., Sætre, R., 1986. Retroflection of Atlantic water in the Norwegian Trench. Deep-Sea Res. 33, 247–265.
Garau, B., Ruiz, S., Zhang, W.G., Pascual, A., Heslop, E., Kerfoot, J., Tintoré, J., 2011. Thermal lag correction on Slocum CTD glider data. J. Atmos. Oceanic Technol. 28, 1065–1071.
ICES report on ocean climate 2018. In: González-Pola, C., Larsen, K.M.H., Fratantoni, P., Beszczynska-Möller, A. (Eds.), ICES Co-Operative Reseach Report No. 349, ICES Co-Operative Reseach Report No. 339.
Graham, J.A., O'Dea, E., Holt, J., Polton, J., Hewitt, H.T., Furner, R., Guihou, K., Brereton, A., Arnold, A., Wakelin, S., Castillo Sanchez, J.M., Gabriela Mayorga Adame, C., 2018. AMM15: a new high-resolution NEMO configuration for operational simulation of the European north-west shelf. Geosci. Model Dev. 11, 681–696.

Green, R.E., Bower, A.S., Lugo-fernández, 2014. First autonomous bio-optical profiling float in the Gulf of Mexico reveals dynamic biogeochemsitry in deep waters. PLOS One 9, e101658.
Hall, R.A., Aslam, T., Huvenne, V.A.I., 2017. Partly standing internal tides in a dendritic submarine canyon observed by an ocean glider. Deep-Sea Res. I 126, 73–84.
Hill, A.E., Brown, J., Fernand, L., Holt, J.T., Horsburgh, K.J., Proctor, R., Raine, R., Turrell, W.R., 2008. Thermohaline circulation of shallow tidal seas. Geophys. Res. Lett. 35, L11605.
Hill, A.E., Horsburgh, K.J., Garvine, R.W., Gillibrand, P.A., Slesser, G., Turrell, W.R., Adams, R.D., 1997. Observations of a density-driven recirculation of the Scottish Coastal Current in the Minch. Estuar. Coast. Shelf Sci. 45, 473–484.
Holliday, N.P., Reid, P.C., 2001. Is there a connection between high transport of water through the Rockall Trough and ecological changes in the North Sea? ICES J. Mar. Sci. 58, 270–274.
Holt, J.T., Proctor, R., 2008. The seasonal circulation and volume transport on the northwest European continental shelf: a fine-resolution model study. J. Geophys. Res. 113, C06021.
Inall, M.E., Gillibrand, P.A., Griffiths, C., MacDougal, N., Blackwell, K., 2009. On the oceanographic variaiblity of the Northwest European shelf to the west of Scotland. J. Mar. Syst. 77, 210–226.
Johnson, D., 2008. Environmental indicators: their utility in meeting the OSPAR Convention's regulatory needs. ICES J. Mar. Sci. 65, 1387–1391.
Lindley, J.A., Roskell, J., Warner, A.J., Halliday, N.C., Hunt, H.G., John, A.W.G., Jonas, T.D., 1990. Doliolids in the German Bight in 1989: evidence for exceptional inflow into the North Sea. J. Mar. Biol. Assoc. U. K. 70, 679–682.
Marsh, R., Haigh, I.D., Cunningham, S.A., Inall, M.E., Porter, M., Moat, B.I., 2017. Large-scale forcing of the European Slope Current and associated inflows to the North Sea. Ocean Sci. 13, 315–335.
Naveira Garabato, A.C., McDonagh, E.L., Stevens, D.P., Heywood, K.J., Sanders, R.J., 2002. On the export of Antarctic Bottom Water from the Weddell Sea. Deep-Sea Res. II 49, 4715–4742.
Otto, L., Zimmerman, J.T.F., Furnes, G.K., Mork, M., Sætre, R., Becker, G., 1990. Review of the physical oceanography of the North Sea. Neth. J. Sea Res. 26 161–138.
Sheehan, P.M.F., Berx, B., Gallego, A., Hall, R.A., Heywood, K.J., Hughes, S.L., 2017. Thermohaline forcing and interannual variability of northwestern inflows into the northern North Sea. Cont. Shelf Res. 138, 120–131.
Sheehan, P.M.F., Berx, B., Gallego, A., Hall, R.A., Heywood, K.J., Hughes, S.L., Queste, B.Y., 2018. Shelf sea tidal currents and mixing fronts determined from ocean glider observations. Ocean Sci. 14, 225–236.
Skogen, M.D., Moll, A., 2005. Importance of ocean circulation in ecological modeling: an example from the North Sea. J. Mar. Syst. 57, 289–300.
Svendsen, E., Sætre, R., Mork, M., 1991. Features of the northern North Sea circulation. Cont. Shelf Res. 5, 493–508.
Taylor, A.H., 1987. Modelling contaminants in the North Sea. Sci. Total Environ. 63, 45–67.
Turrell, W.R., 1992. New hypotheses concerning the circulation of the northern North Sea and its relation to North Sea fish stock recruitment. ICES J. Mar. Sci. 49, 107–123.
Turrell, W.R., Henderson, E.W., 1990. Transport events within the Fair Isle Current during the Autumn Circulation Experiment. Estuar. Coast. Shelf Sci. 31, 25–44.
Turrell, W.R., Henderson, E.W., Slesser, G., 1990. Residual transport within the Fair Isle Current observed during the Autumn Circulation Experiment (ACE). Cont. Shelf Res. 10, 521–543.
Turrell, W.R., Henderson, E.W., Slesser, G., Payne, R., Adams, R.D., 1992. Seasonal changes in the circulation of the northern North Sea. Cont. Shelf Res. 12, 257–286.
Turrell, W.R., Slesser, G., Payne, R., Adams, R.D., Gillibrand, P.A., 1996. Hydrography of the East Shetland Basin in relation to decadal North Sea variability. ICES J. Mar. Sci. 53, 899–916.
Winther, N.G., Johannessen, J.A., 2006. North Sea circulation: Atlantic inflow and its destination. J. Geophys. Res. 111, C12018.